Photoinitiated Predissociation of the NO Dimer in the Region of the Second and Third NO Stretch Overtones†

A. B. Potter, J. Wei, and H. Reisler*

Department of Chemistry, University of Southern California, Los Angeles, California 90089-0482

Received: August 20, 2004; In Final Form: November 1, 2004

Photofragment yield spectra and NO($X^2\Pi_{1/2,3/2}$; $v = 1, 2, 3$) product vibrational, rotational, and spin−orbit state distributions were measured following NO dimer excitation in the 4000−7400 cm^{-1} region in a molecular beam. Photofragment yield spectra were obtained by monitoring NO($X^2\Pi$; $v = 1, 2, 3$) dissociation products via resonance-enhanced multiphoton ionization. New bands that include the symmetric ν_1 and asymmetric ν_5 NO stretch modes were observed and assigned as $3\nu_5$, $2\nu_1 + \nu_5$, $\nu_1 + 3\nu_5$, and $3\nu_1 + \nu_5$. Dissociation occurs primarily via $\Delta v = -1$ processes with vibrational energy confined preferentially to one of the two NO fragments. The vibrationally excited fragments are born with less rotational energy than predicted statistically, and fragments formed via $\Delta v = -2$ processes have a higher rotational temperature than those produced via $\Delta v = -1$ processes. The rotational excitation likely derives from the transformation of low-lying bending and torsional vibrational levels in the dimer into product rotational states. The NO spin−orbit state distribution reveals a slight preference for the ground $^2\Pi_{1/2}$ state, and in analogy with previous results, it is suggested that the predominant channel is $X^2\Pi_{1/2} + X^2\Pi_{3/2}$. It is suggested that the long-range potential in the N−N coordinate is the locus of nonadiabatic transitions to electronic states correlating with excited product spin−orbit states. No evidence of direct excitation to electronic states whose vertical energies lie in the investigated energy region is obtained.

I. Introduction

The nitric oxide dimer, a weakly covalently bound complex, is an intriguing system for studies of photodissociation dynamics. The ground state of $(NO)_2$ is formed by the pairing of two π^* orbitals on NO, leading to a weak (710 ± 10 cm^{-1}) but covalent N−N bond. Evidence of the chemical nature of the intermolecular bond is seen in ab initio calculations, as well as in experimental examinations of the strong and broad UV absorption that peaks at 205 nm.[1−6] The equilibrium geometry of gas-phase $(NO)_2$ has been determined by microwave spectroscopy to be a trapezoidal cis-planar structure.[7,8] The N−O bond length is 1.161 Å, the N−N bond is 2.236 Å, and the ONN angle is 99.6°. Because of the disparity between the strengths of the N−O and N−N bonds, dissociation following excitation of N−O stretch vibrations in the dimer displays evidence of restricted intramolecular vibrational energy distribution (IVR), as often associated with predissociation of van der Waals complexes.[9−17]

Vibrational predissociation following N−O stretch excitation in the ground electronic state has been studied both experimentally and theoretically.[11−17] In a comprehensive series of studies, Casassa et al. have found that the lifetimes of the ν_1 symmetric (1868 cm^{-1}) and ν_5 asymmetric (1789 cm^{-1}) N−O stretch modes are different: 880 ± 260 and 39 ± 8 ps, respectively.[13] Dissociation fragments are produced with 70−80% of the available energy deposited into translation, with up to 12% in product rotation. In the first overtone region, the lifetimes of the $\nu_1 + \nu_5$ and $2\nu_5$ states are 34 ± 6 and 20 ± 3 ps, respectively,[17] and one of the NO($X^2\Pi$) products is preferentially in $v = 1$. Only 3% of the remaining available energy is deposited in fragment rotation. Dissociation fragments appear in both spin−orbit states, mostly as NO($X^2\Pi_{1/2}$) + NO($X^2\Pi_{3/2}$) pairs, but with contributions also from the NO($X^2\Pi_{1/2}$) + NO($X^2\Pi_{1/2}$) channel. Two mechanisms have been considered in explaining the energy disposal: electronically nonadiabatic vibrational predissociation and vibrational potential coupling that occurs solely on the ground-state surface.[13,17] Additionally, a hybrid mechanism has been proposed in which the total dissociation rate is determined predominantly by nonadiabatic crossings, while partial rates to specific product channels are affected by further vibrational potential coupling.[16]

The issue of the participation of excited electronic states in the dissociation is intriguing, because seven excited electronic states correlating with two NO($X^2\Pi$) fragments are calculated to lie in the region below 8000 cm^{-1} (1 eV). The vertical excitation energy of the lowest state was recently calculated by Tobita et al. at 1498 cm^{-1}; the highest is at 7425 cm^{-1}.[1] On the basis of their microwave and radio frequency spectra, Western et al. inferred the existence of low-lying singlet state(s) correlating with ground-state products from differences between expected and observed spin-rotation coupling constants.[8] They estimated the average excitation energy of this state(s) at ∼4500 cm^{-1}, clearly within the range of the electronic states calculated ab initio. In an absorption spectrum of liquid NO, Mason observed a rising IR absorption beginning at 1160 nm (8620 cm^{-1}), which was assigned to NO dimer electronic transitions.[18]

The ground-state infrared spectroscopy of $(NO)_2$ in the N−O stretch region has been investigated as well.[19−29] The 1600−4000 cm^{-1} gas-phase spectrum was characterized by Dinerman and Ewing at 77−150 K, allowing them to assign both N−O fundamental stretches, the first asymmetric stretch overtone and

* Corresponding author. E-mail: reisler@usc.edu.

† Part of the special issue "George W. Flynn Festschrift".

10.1021/jp046226w CCC: $30.25
Published on Web 02/01/2005

the first combination band.[22] These assignments were further refined by Menoux et al. in the 1800−3700 cm^{-1} region.[27] Matrix spectroscopy up to 6000 cm^{-1} in argon and nitrogen matrices revealed the presence of $2\nu_5$, $\nu_1 + \nu_5$, and in the case of argon matrix spectroscopy also $2\nu_1$.[30,31] Neither study reported $(NO)_2$ absorptions to higher N−O stretch overtones. Nour et al. measured the Raman spectrum of solid $(NO)_2$ and characterized ν_1 as a nearly pure N−O stretching mode, while ν_5 exhibited stronger coupling to the ν_3 in-plane bend.[32] More recent force constant calculations by Krim and Lacome demonstrated that ν_1 possesses 99.7% N−O stretch character, while the ν_5 normal mode is composed of 82.4% N−O stretch and 17.6% bend.[31] This result led the authors to conclude that ν_5 provides a faster channel of predissociation than ν_1, as it facilitates coupling between the N−O asymmetric stretch and the N−N stretch via the ONN bend. In addition to gas-phase and matrix studies, spectral features at 3708 and 3515 cm^{-1} of liquid NO were attributed to NO stretch vibrations of $(NO)_2$.[18] In that study, the presence of a second NO stretch overtone at ~5200 cm^{-1} was also suggested.

The goal of the present study is to further investigate the nonadiabatic transitions between electronic states following overtone excitation in the NO dimer. Specifically, we wish to distinguish between long-range interactions that happen in the asymptotic region of the potential and lead to excited spin−orbit states of NO, nonadiabatic interactions in the Franck−Condon vertical region, and direct excitation to excited electronic states. We also wish to explore patterns in energy disposal that shed light on the predissociation mechanism. To this end, we carried out measurements in the molecular beam of the spectroscopy and predissociation of $(NO)_2$ at 4000−7400 cm^{-1}, covering the region of the second and third NO stretch overtones. The measured spectra reveal the presence of previously unobserved NO stretch overtones and combination bands. The vibrational and rotational state distributions of product $NO(X^2\Pi_{1/2,3/2})$ are determined and compared with previously observed $(NO)_2$ predissociation dynamics from lower vibrational levels of the ground and excited electronic states. The picture that emerges is similar to that of vibrational predissociation of van der Waals dimers, with nonadiabatic interactions in the exit channel resulting in population of both NO spin−orbit states.

II. Experimental Methods

The experiments are performed using a seeded supersonic molecular beam of $(NO)_2$ and laser infrared photodissociation of the dimer. Following dissociation, the vibrationally excited NO fragments are ionized by resonance-enhanced multiphoton ionization (REMPI) and detected by time-of-flight (TOF) mass spectroscopy.

The vacuum chamber consists of two differentially pumped chambers, the source chamber and the detection chamber, which are joined by a skimmer-equipped flange.[33] Both chambers are evacuated by turbomolecular pumps. The piezoelectric pulse nozzle is mounted ~30 mm from the skimmer (Beam Dynamics, 1.51 mm diameter) in the source chamber. With the nozzle operating at 10 Hz, the pressure in the detection region is $\sim 4 \times 10^{-7}$ Torr.

Nitric oxide dimer is formed in a free-jet expansion of NO in a 70%:30% Ne:He gas buffer. A pulsed molecular beam containing up to 20% NO in 2 atm of the carrier gas propagates through the skimmer into the detection chamber. The molecular beam is crossed in the photodissociation region by coaxial pulsed IR photolysis and UV detection laser beams, which intersect the molecular beam at right angles. Following photodissociation, state-selected $NO(X^2\Pi; v)$ fragments are ionized and accelerated vertically toward a 1 in. diameter microchannel plate (MCP) detector through a Wiley−McLaren TOF mass spectrometer. The mass spectrometer separates $m/e = 30$ and 60 (corresponding to NO and $(NO)_2$, respectively). The $(NO)_2$ yield is determined by monitoring the mass spectrum during one-color nonresonant ionization at 280 nm. Under these experimental conditions, no clusters higher than dimer are observed. An estimate of the rotational temperature, $T_{rot} = 4$ K, in the molecular beam is obtained by measuring the REMPI spectrum of the NO $A^2\Sigma^+(v = 0) \leftarrow X^2\Pi(v = 0)$ transition in mixtures of 1% NO. This estimate is in agreement with the $(NO)_2$ rotational temperatures determined from simulations of the experimental NO photofragment yield spectra obtained by vibrational excitation of the NO dimer (see section III).

The IR photolysis radiation is obtained from a Nd:YAG laser-pumped OPO−OPA system (LaserVision, 0.4 cm^{-1} bandwidth). The laser operates in the 4000−7400 cm^{-1} region with an output of 7.5−22 mJ. The IR wavelength was calibrated using the photoacoustic spectrum of methane.[34] The beam is steered to the chamber with CaF_2 optics and focused using a $f = 20$ cm lens. The UV detection pulse is generated by frequency doubling the output of a Nd:YAG pumped dye laser system (Coumarin 480 and LD498, 0.2 cm^{-1} bandwidth). The laser wavelength is tuned to the NO $A^2\Sigma^+(v = 0) \leftarrow X^2\Pi(v = 1, 2, 3)$ transitions at 236.2, 247.0, and 258.7 nm, respectively. To avoid multiphoton dissociative ionization of $(NO)_2$ with the UV pulse (and saturation of the MCP detector signal),[9] the detection laser intensity is kept below 0.1 mJ and is only mildly focused ($f =$ 40 cm). Both the pump and probe beams have parallel polarization (i.e., in the plane of the molecular and laser beams). The REMPI spectra are converted to rotational state populations by using line strength appropriate for saturated transitions (see section III).

Following photodissociation, every energetically allowed NO fragment vibrational level except $NO(X^2\Pi; v = 0)$ can be detected. The $v = 0$ dissociation fragments cannot be monitored because the UV wavelength necessary for their REMPI detection is strongly absorbed by $(NO)_2$ (which undergoes UV absorption at wavelengths <242 nm), generating a large background ion signal.

In the case of $NO(X^2\Pi; v = 1)$ detection, the frequency of the detection laser pulse is above the threshold for UV electronic absorption in $(NO)_2$. Even in the absence of the IR laser radiation, our current experiments show some background of $NO(X^2\Pi_{1/2}; v = 1)$, possibly from two-photon dissociative ionization,[9] which is much colder rotationally than the corresponding fragment from IR photodissociation and cannot be completely suppressed. Therefore, we optimize the IR + UV product signal by monitoring the $NO(X^2\Pi_{3/2})$ fragment, which is not observed in UV-only photodissociation. The contribution of $NO(X^2\Pi_{1/2})$ from dissociative ionization is minimized by maintaining low intensity of the UV pulse. Additionally, the UV detection pulse is delayed by ≥10 ns relative to the IR photolysis pulse to avoid depleting the $(NO)_2$ ground-state vibrational population with UV excitation. There is no background signal in the region of $NO(X^2\Pi_{1/2,3/2}; v = 2, 3)$ detection.

Two types of experiments are performed. First, NO photofragment yield spectra are acquired by scanning the photolysis laser with the detection laser fixed at specific bandhead wavelengths to detect selectively $NO(X^2\Pi_{3/2}; v = 1, 2, 3)$ by 1 + 1 REMPI. Each point in the spectrum represents the sum of signals from 30 laser firings. The IR laser intensity is kept constant throughout the region of the observed spectral bands.

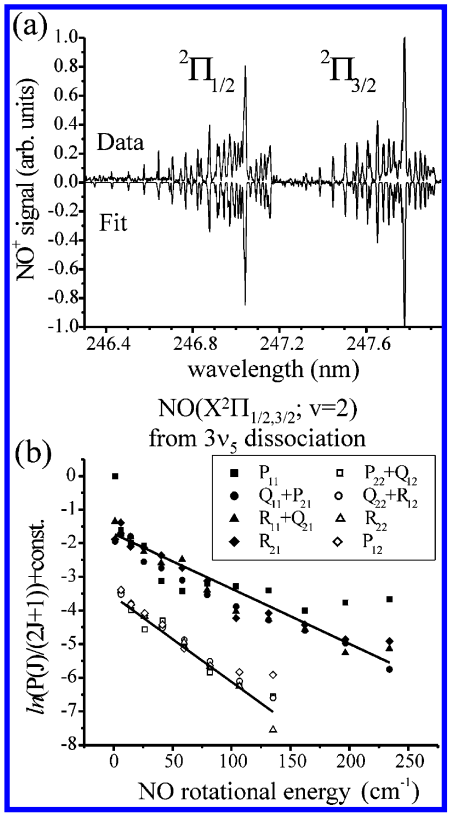

Figure 1. (a) NO $A^2\Sigma^+(v = 0) \leftarrow X^2\Pi(v = 2)$ REMPI spectrum following $3\nu_5$ dissociation. The top plot is the experimental spectrum, and the bottom is the fit to the data. (b) Boltzmann plots of the NO($X^2\Pi_{1/2,3/2}$; $v = 2$) fragment rotational state distributions extracted from the above spectrum. The closed and open symbols correspond to the $\Pi_{1/2}$ and $\Pi_{3/2}$ spin−orbit states, respectively. The solid line corresponds to the linear least-squares fit to the data, as described in the text.

In typical measurements, the delay between the photolysis and detection laser pulses is maintained at ∼10 ns. In experiments aimed at detecting longer living excited states, the delay between the laser pulses is increased to 50 ns. In the second type of experiments, the REMPI spectra of the fragments are measured by fixing the photolysis pulse at the maximum of the IR absorption feature while scanning the detection laser frequency through the selected $A^2\Sigma^+(v = 0) \leftarrow X^2\Pi(v = 1, 2, 3)$ transition.

To determine the rotational state distributions of $v \neq 0$ NO products, the REMPI spectra are fit by using a set of Gaussian basis functions which reproduces the resolved peaks well. Each basis function has the experimentally measured 0.4 cm^{-1} line width and is centered at the calculated rotational line position for the $A^2\Sigma^+(v = 0) \leftarrow X^2\Pi(v = 1, 2, 3)$ transition. The spectral line intensities are determined by a least-squares fit using Tikhonov regularization,[35] a procedure that stabilizes the line intensities in the overlapped region of the spectrum. The line intensities, each corresponding to a specific NO(A←X) rovibronic transition, are determined for each spectral branch. Rotational populations are calculated from the intensities by using linestrengths for fully saturated conditions in the REMPI detection. The observed linewidth of 0.4 cm^{-1}, which is greater than the laser bandwidth (0.2 cm^{-1}), supports the saturation assumption.

An example of the experimental REMPI spectrum for NO($X^2\Pi$; $v = 2$), obtained following 5299.1 cm^{-1} excitation and its fit, is shown in Figure 1a. Figure 1b shows NO($X^2\Pi$; $v = 2$) rotational state populations obtained by analysis of each spectral branch and plotted as $\ln[P(J)/(2J + 1)]$ vs NO rotational energy $E_{rot}(J)$ (a Boltzmann plot). We find that similar slopes are obtained when different branches are used, confirming that the spectra are indeed obtained under saturation conditions and alignment effects can be neglected. The final rotational distribution is generated by averaging the population of each J state obtained by using branch lines that are not too severely overlapped. The solid lines in Figure 1b show least-squares fits to the Boltzmann plots from which the rotational temperature is generated. The spin−orbit population ratios for each observed NO($X^2\Pi$; v) dissociation product following excitation of each $(NO)_2$ vibrational level are obtained from integration of the rotational state distributions for each product spin−orbit state.

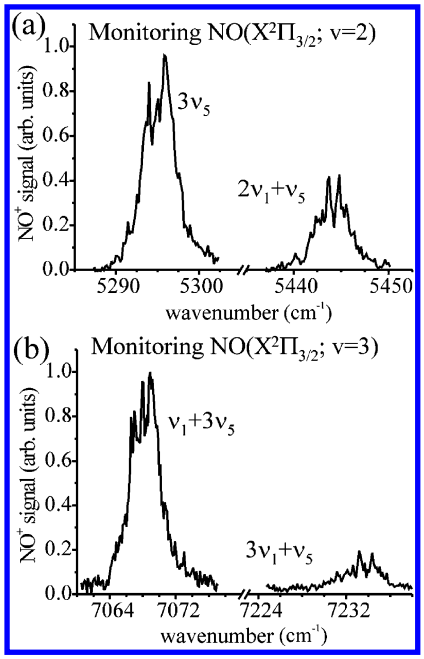

Figure 2. Photofragment yield spectra obtained by monitoring (a) NO($X\ ^2\Pi_{3/2}$; $v = 2$) and (b) NO($X\ ^2\Pi_{3/2}$; $v = 3$).

Product vibrational distributions are calculated from the measured yield spectra in two steps. First, the rovibrational spectrum for each $(NO)_2$ vibrational band, obtained under unsaturated conditions, is integrated and normalized by the Franck−Condon factors of the monitored NO $A^2\Sigma^+(v = 0) \leftarrow X^2\Pi_{3/2}(v = 1, 2, 3)$ transition[36] and the fraction of the NO($X^2\Pi_{3/2}$; v) product distribution that is ionized by the detection laser at the bandhead frequency. In the second step, the final NO product vibrational distribution is determined by including the population of the $^2\Pi_{1/2}$ state, obtained from the $^2\Pi_{1/2}/^2\Pi_{3/2}$ ratios. The errors in the vibrational distributions represent primarily the precision in the laser alignment, which is optimized for each measurement, and variations in laser intensity at the multiple detection frequencies needed to detect the different NO($X^2\Pi$; v) states.

III. Results and Analysis

Assignment of Vibrational Transitions of the NO Dimer. Photofragment yield spectra were obtained for each product NO($X^2\Pi$; $v = 1, 2, 3$) state that could be detected. Although the full 4000−7400 cm^{-1} range was scanned and the delay increased to 50 ns, only the vibrational transitions shown in Figure 2 were observed. *cis*-$(NO)_2$ has C_{2v} symmetry with the molecule in the $a-b$ plane and the C_2 rotation axis along the b-axis. Therefore, rovibrational a-type transitions are expected to upper levels of b_2 symmetry, and b-type bands are expected for upper levels of a_1 symmetry.

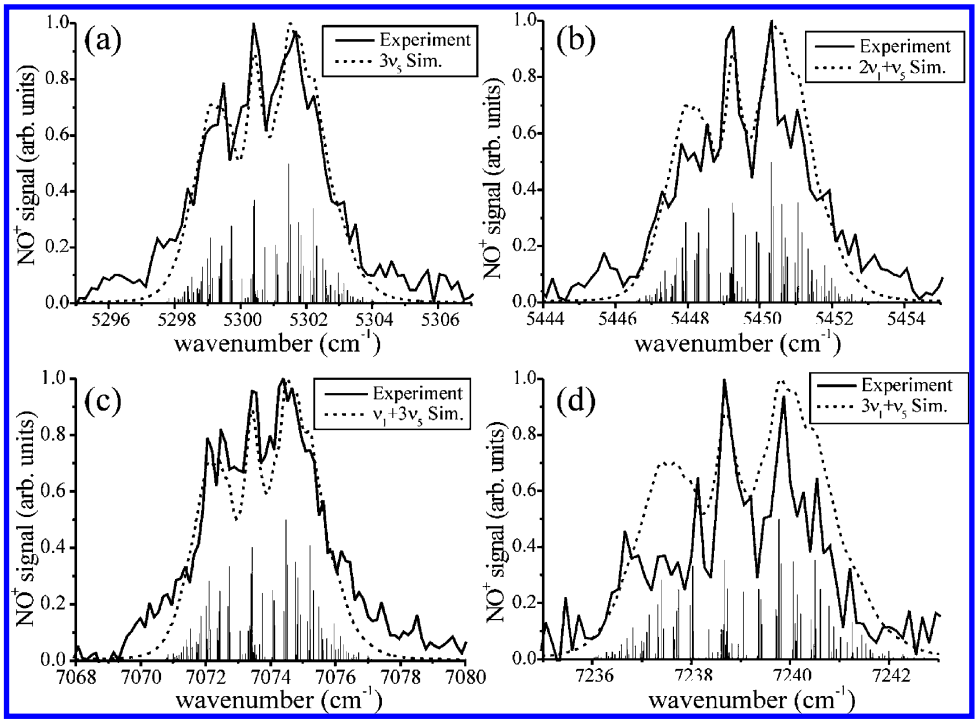

Figure 3. Simulated *a*-type rotational spectra for the (a) $3\nu_5$, (b) $2\nu_1 + \nu_5$, (c) $\nu_1 + 3\nu_5$, and (d) $3\nu_1 + \nu_5$ vibrational transitions. The solid and dashed plots correspond to the experimental and simulated spectra, respectively. The rotational stick spectra are also shown for comparison. See the text for details of the simulations.

TABLE 1: Transition Assignments and Comparisons with Calculations[a]

assignment	observed origin (cm^{-1})	calculated origin (cm^{-1})	exp − calc (cm^{-1})
ν_5	1789.10[b]	1790.34	−1.24
ν_1	1868.25[c]	1868.49	−0.24
$2\nu_5$	3559.32[d]	3559.32	1.01
$\nu_1 + \nu_5$	3626.45[d]	3626.47	−0.02
$3\nu_5$	5300.4 ± 0.4[e]	5303.9	−3.5
$2\nu_1 + \nu_5$	5449.3 ± 0.4[e]	5443.3	6.0
$\nu_1 + 3\nu_5$	7073.4 ± 0.4[e]	7075.3	−1.9
$3\nu_1 + \nu_5$	7238.7 ± 0.4[e]	7240.7	−2.0

[a] The harmonic frequencies and anharmonicity constants determined from this analysis are $\omega_1 = 1878.2$, $\omega_5 = 1801.5$, $\chi_{11} = -9.67$, $\chi_{55} = -11.19$, and $\chi_{15} = -32.36$ cm^{-1}. [b] Reference 28. [c] Reference 29. [d] Reference 17. [e] This work.

The band origins were determined from spectral simulations. The new transitions observed in this work were simulated as *a*-type transitions (see Figure 3) by using the simulation program ASYROT.[37] In the simulations, published ground-state rotational constants were used,[8] whereas the upper state rotational constants were approximated using the average of the previously determined values derived for $2\nu_5$ and $\nu_1 + \nu_5$.[17] The spectral resolution of the measured bands is insufficient for accurate determination of upper state rotational constants and their variation with excitation energy. However, values of the band origins are not affected significantly by small changes in rotational constants. The derived band origins are listed in Table 1.

Simulations such as those shown in Figure 3 were obtained for $T = 4 \pm 1$ K and convoluted with a Voigt profile. The Gaussian component of the linewidth was set at the 0.4 cm^{-1} IR laser bandwidth, and it dominated the spectrum. The Lorentzian component that best fits the data has a width of 0.2 ± 0.1 cm^{-1}, corresponding to a lifetime of 36 ± 17 ps. This value is similar to those measured previously for $2\nu_5$ and $\nu_1 + \nu_5$.[17] Simulations in the ranges given by the error bars reproduced best both the overall widths of the vibrational bands and the shapes (peaks and valleys) of the structural features within each band. Although both increased temperature and Lorentzian width cause broadening of the spectral features, only combinations within the ranges specified above give acceptable simulations of the data.

In summary, all the observed bands could be simulated by *a*-type transitions without a significant change in rotational constants or Lorentzian linewidth. Only the weak band around 7200 cm^{-1} could not be characterized exclusively as an *a*- or *b*-type band, because of its poor signal-to-noise ratio.

To assign the new transitions, we performed a normal-mode analysis including the known fundamental and first overtone band origins of the asymmetric N−O stretch (ν_5), the N−O symmetric stretch (ν_1), and the $\nu_1 + \nu_5$ combination band as well as the observed transitions from this work.[17,24,28] The assignments and comparisons of experimental with calculated values are listed in Table 1. The new bands are tentatively assigned as $3\nu_5$, $2\nu_1 + \nu_5$, $\nu_1 + 3\nu_5$, and $3\nu_1 + \nu_5$. The harmonic frequencies and anharmonicity constants determined from this analysis are $\omega_1 = 1878.2$, $\omega_5 = 1801.5$, $\chi_{11} = -9.67$, $\chi_{55} = -11.19$, and $\chi_{15} = -32.36$ cm^{-1}. It should be noted that the normal-mode analysis used in this assignment, while valid at low vibrational excitation, is increasingly inadequate for higher overtones. However, the observed band origins agree rather well with the normal-mode calculations; moreover, all the upper vibrational states have b_2 symmetry, consistent with observation of only *a*-type bands.

Because the vibrational spectra are obtained by measuring yields of NO($X^2\Pi$; $v = 1, 2, 3$) products rather than by direct absorption measurements, we cannot preclude the possibility that other overtone or combination bands of $(NO)_2$ are excited, but either their lifetimes are longer than the maximum time delays achieved in our experiments (50 ns) or dissociation from these bands generates only NO($X^2\Pi$; $v = 0$) + NO($X^2\Pi$; $v = 0$). Additionally, we searched but did not find evidence for broad resonances that could be attributed to direct absorption to

repulsive electronic states, which according to theory should lie in this region (the calculated oscillator strength is 2×10^{-6}).[2]

NO($X^2\Pi$; $v = 1, 2, 3$) Photofragment Yields. Following dissociation from the N−O stretch second overtone region of $(NO)_2$ [$3\nu_5$ and $2\nu_1 + \nu_5$, henceforth referred to as $(NO)_2(m = 3)$ to denote three quanta of NO stretch], NO($X^2\Pi$) fragment vibrational levels $v = 0$, 1, 2 are energetically accessible and $v = 1$, 2 are monitored [i.e., NO($v = m - 2$) and NO($v = m - 1$), respectively]. Representative photofragment yield spectra are shown in Figure 2. Integration and normalization of the spectra obtained by monitoring $v = 1$ and 2 (as described in section II) give relative populations $P(v = 2)/P(v = 1) = 0.97 \pm 0.30$ and 7.3 ± 0.7 for dissociation from $3\nu_5$ and $2\nu_1 + \nu_5$, respectively. The errors in these measurements represent the spread in results of multiple measurements and the accuracy of the spin−orbit state distributions. Taking into account the ground-state dissociation energy of $(NO)_2$,[38] four channels are energetically accessible following $(NO)_2(m = 3)$ dissociation:

$$(NO)_2(m = 3) \rightarrow NO(X^2\Pi;\, v = 2) + NO(X^2\Pi;\, v = 0) \quad (1)$$

$$\rightarrow NO(X^2\Pi;\, v = 1) + NO(X^2\Pi;\, v = 1) \quad (2)$$

$$\rightarrow NO(X^2\Pi;\, v = 1) + NO(X^2\Pi;\, v = 0) \quad (3)$$

$$\rightarrow NO(X^2\Pi;\, v = 0) + NO(X^2\Pi;\, v = 0) \quad (4)$$

where channels 1 and 2 represent $\Delta v = -1$ dissociation and channels 3 and 4 represent $\Delta v = -2$ and $\Delta v = -3$ processes, respectively. For each channel, both spin−orbit states for each NO fragment are energetically allowed.

Dissociation via $2\nu_1 + \nu_5$ clearly favors channel 1, indicating that $\Delta v = -1$ is the predominant pathway. Due to the nature of the experiments, we cannot distinguish between NO($X^2\Pi$; $v = 1$) fragments formed via channels 2 and 3. We are also unable to detect NO($X^2\Pi$; $v = 0$); however, considering that $P(v = 1)$ is much smaller than $P(v = 2)$, a significant contribution from channel 4 is unlikely. On the other hand, with $3\nu_5$ dissociation, $P(v = 2)$ and $P(v = 1)$ are nearly identical, suggesting that dissociation from $3\nu_5$ proceeds via a somewhat different pathway than $\nu_1 + 2\nu_5$, and that both $\Delta v = -1$ and $\Delta v = -2$ NO($X^2\Pi$; $v = 1$) producing processes (i.e., channels 2 and 3) may be important (see section IV).

Dissociation from states in the N−O stretch third overtone region of $(NO)_2$ [$\nu_1 + 3\nu_5$ and $3\nu_1 + \nu_5$, henceforth referred to as $(NO)_2(m = 4)$] can produce NO($X^2\Pi$; $v = 0$, 1, 2, 3) fragments. Six channels are energetically possible:

$$(NO)_2(m = 4) \rightarrow NO(X^2\Pi;\, v = 3) + NO(X^2\Pi;\, v = 0) \quad (5)$$

$$\rightarrow NO(X^2\Pi;\, v = 2) + NO(X^2\Pi;\, v = 1) \quad (6)$$

$$\rightarrow NO(X^2\Pi;\, v = 2) + NO(X^2\Pi;\, v = 0) \quad (7)$$

$$\rightarrow NO(X^2\Pi;\, v = 1) + NO(X^2\Pi;\, v = 1) \quad (8)$$

$$\rightarrow NO(X^2\Pi;\, v = 1) + NO(X^2\Pi;\, v = 0) \quad (9)$$

$$\rightarrow NO(X^2\Pi;\, v = 0) + NO(X^2\Pi;\, v = 0) \quad (10)$$

Unlike $(NO)_2(m = 3)$ dissociation, some of these channels can be eliminated on the basis of the experimental observations. In both $\nu_1 + 3\nu_5$ and $3\nu_1 + \nu_5$ dissociation, no signal from NO($X^2\Pi$; $v = 1$) can be detected; therefore, channels 6, 8, and 9 are eliminated. Integration and normalization of the NO($X^2\Pi$; $v = 3$) and NO($X^2\Pi$; $v = 2$) signals [i.e., NO($v = m - 1$) and NO($v = m - 2$), respectively] give relative populations $P(v = 3)/P(v = 2) = 5.7 \pm 0.7$ for $\nu_1 + 3\nu_5$, indicating that the major channel is 5 ($\Delta v = -1$), followed by 7 ($\Delta v = -2$). Again, we cannot detect NO($X^2\Pi$; $v = 0$), but considering that NO($X^2\Pi$; $v = 1$) is not produced in detectable amounts, channel 10 seems unlikely. Following $3\nu_1 + \nu_5$ dissociation, only NO($X^2\Pi$; $v = 3$) can be detected [$P(v = 3)/P(v = 2) > 10$], eliminating every channel except channel 5. This suggests that $\Delta v = -1$ is the dominant pathway.

Product Spin−Orbit State Ratios. Spin−orbit state ratios, $[^2\Pi_{1/2}]/[^2\Pi_{3/2}]$, for each observed NO($X^2\Pi$; v) fragment following dissociation from the $(NO)_2$ vibrational level are listed in Table 2. The ratio in most cases is near unity, with a slight preference for the ground $^2\Pi_{1/2}$ state. The exception is dissociation via $3\nu_1 + \nu_5$, which shows a strong preference for $^2\Pi_{1/2}$. Previous studies of $(NO)_2(m = 1, 2)$ predissociation[13,17] showed that the main spin−orbit channels were NO($\Pi_{1/2}$) + NO($\Pi_{3/2}$) and NO($\Pi_{1/2}$) + NO($\Pi_{1/2}$). Because in almost all cases $[\Pi_{1/2}]/[\Pi_{3/2}] > 1$, we assume, in analogy with previous findings, that the excess $[\Pi_{1/2}]$ derives only from the $\Pi_{1/2} + \Pi_{1/2}$ channel (i.e., the $\Pi_{3/2} + \Pi_{3/2}$ channel is neglected).

Product NO($X^2\Pi_{1/2,3/2}$; $v = 1, 2, 3$) Rotational Distributions. Boltzmann plots [$\ln[P(J)/(2J + 1)]$ vs $E_{rot}(J)$] of product rotational state distributions are shown in Figure 4. All give fairly good straight lines, and rotational temperatures are derived from the slopes of the least-squares linear fits as a measure of the rotational excitation. Rotational temperatures for both the NO($v = m - 1$) and NO($v = m - 2$) fragments are listed in Table 2 for $m = 3$ and 4. The percent of energy deposited in rotation for each dissociation channel is summarized in Table 3. To obtain this estimate, two assumptions are made. First, as described above, we assume that only the $\Pi_{1/2} + \Pi_{3/2}$ and $\Pi_{1/2} + \Pi_{1/2}$ channels are populated. Second, it is assumed that the unobserved NO($X^2\Pi$; $v = 0$) cofragment in each channel is produced with the same amount of rotational energy as the observed NO($X^2\Pi$; $v = 1$, 2, 3) fragment. This assumption is reasonable when the rotational excitation is low and derives mainly from transformation of low-lying bending and torsional levels into rotational wave functions (see section IV). The average rotational energy per fragment is determined from the rotational temperature as $\langle E_{rot} \rangle = kT_{rot}$.

IV. Discussion

Spectroscopy and Photophysics. The rovibrational bands assigned in this study were obtained by detecting NO($v > 0$) photofragments. Vibrational levels correlating with two NO($v = 0$) fragments could not be observed, and therefore, the assignments given in Table 1 are based only on partial observations and are considered tentative. For example, it is not clear why the $4\nu_5$ band is not observed. It should also be borne in mind that a normal-mode basis was used in the analysis. Although this treatment is valid at low excitation energies, it should start to fail for high overtones, especially considering the long N−N bond in the NO dimer (2.236 Å), which may hinder coupling between the two NO bonds. A more complete treatment of the spectroscopy should await measurement of the full absorption spectrum in this region. For the purpose of the present discussion, however, we consider the agreement between the experimental and calculated band origins satisfactory, and in the discussion we use the assignments given in Table 1.

We also note that no significant broadening of the bands with increasing vibrational excitation is observed, and a similar Lorentzian width, corresponding to a lifetime of 20−50 ps, satisfactorily simulates all the bands in the $(NO)_2(m = 2-4)$

TABLE 2: Energy Disposal following $(NO)_2(m = 3, 4)$ Dissociation[a]

	$m = 3$		$m = 4$	
normal mode	$3\nu_5$	$2\nu_1 + \nu_5$	$\nu_1 + 3\nu_5$	$3\nu_1 + \nu_5$
well depth (cm^{-1})[b]	953.3 ± 0.4	860.6 ± 0.4	971.8 ± 0.4	891.0 ± 0.4
$P(v = m - 1)/P(v = m - 2)$	0.97 ± 0.3	7.3 ± 0.7	5.7 ± 0.7	>10
T_{rot} ($\Pi_{1/2}$, $v = m - 1$) (K)	88.1 ± 5.8	118.1 ± 7.2	92.7 ± 8.9	184.6 ± 21.4
T_{rot} ($\Pi_{3/2}$, $v = m - 1$) (K)	56.5 ± 2.2	83.0 ± 2.9	62.6 ± 5.9	170.3 ± 27.0
$[\Pi_{1/2}]/[\Pi_{3/2}]$ ($v = m - 1$)	1.21 ± 0.12	1.39 ± 0.13	1.64 ± 0.17	7.62 ± 0.76
T_{rot} ($\Pi_{1/2}$, $v = m - 2$) (K)	141.7 ± 24.3	70.2 ± 5.2	401.7 ± 47.6	
T_{rot} ($\Pi_{3/2}$, $v = m - 2$) (K)	199.7 ± 27.3	126.0 ± 13.8	540.8 ± 94.0	
$[\Pi_{1/2}]/[\Pi_{3/2}]$ ($v = m - 2$)	1.13 ± 0.11	0.89 ± 0.12	1.57 ± 0.42	

[a] m denotes the total number of NO stretch quanta in the vibrational state of the dimer. [b] The well depth is the energy difference between the separated NO fragments and the observed vibrational transition in $(NO)_2$. See text for details.

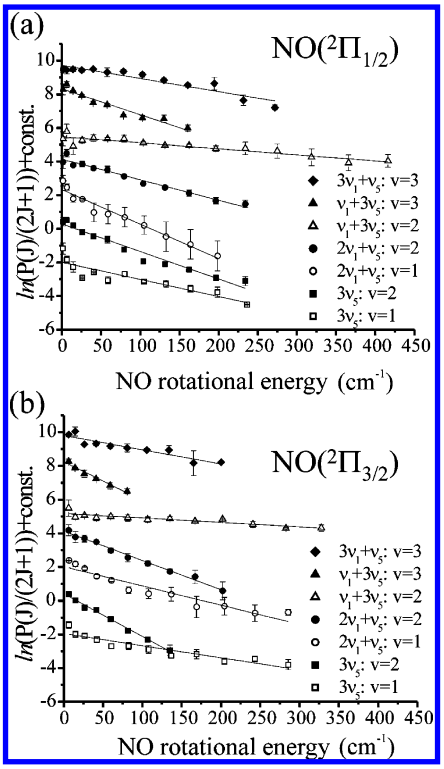

Figure 4. Boltzmann plots for the (a) $NO(X^2\Pi_{1/2}; v)$ and (b) $NO(X^2\Pi_{3/2}; v)$ fragments following dissociation from different vibrational transitions. The solid line corresponds to a linear least-squares fit to the data, and the slope is proportional to the rotational temperature of the fragment. The NO dimer and NO vibrational levels that correspond to each plot are given next to each symbol.

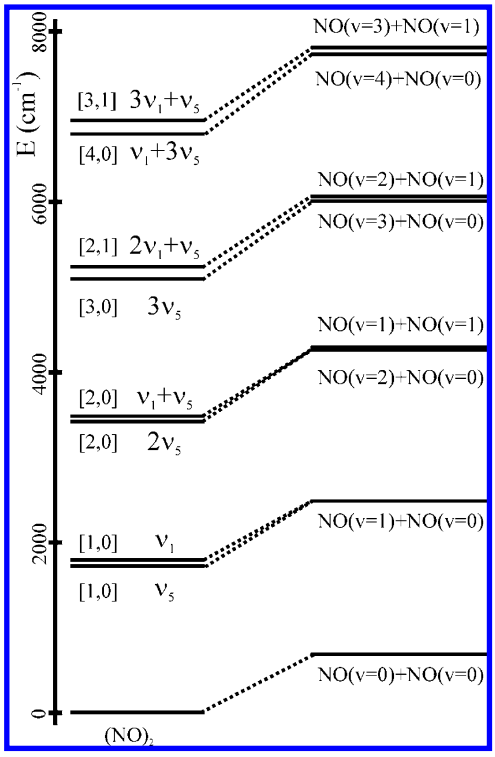

Figure 5. Schematic diagram showing the correlation between the separated $NO(v_a) + NO(v_b)$ fragment channels and the observed $(NO)_2$ N−O stretch vibrations. Both normal- and local-mode vibrational assignments are marked. The corresponding well depths are given in Table 2.

TABLE 3: Estimated Average Rotational Energy in $NO(v_a)$ and $NO(v_b)$[a]

$(NO)_2$ (v)	v_a	v_b	$E_{avl}([\Pi_{1/2}] + [\Pi_{3/2}])$ (cm^{-1})	$<E_{rot}>/E_{avl}$ (%)
$3\nu_5$	1	0	2588.2	9
	1	1	712.4	32
	2	0	740.3	14
$2\nu_1 + \nu_5$	1	0	2739.6	5
	1	1	863.8	17
	2	0	891.7	16
$\nu_1 + 3\nu_5$	2	0	2513.7	24
	3	0	693.9	16
$3\nu_1 + \nu_5$	3	0	859.9	26

[a] The estimates were obtained assuming that only the $\Pi_{1/2} + \Pi_{1/2}$ and $\Pi_{1/2} + \Pi_{3/2}$ channels are significant and that the rotational temperatures of $NO(v_a)$ and $NO(v_b)$ are similar.

region. Thus, no evidence of state-specific strong couplings to excited electronic states is obtained. Rather, the predissociation rates appear to be determined mostly by the coupling between the NO and N−N stretch coordinates, either directly or via the ONN bend, as is typical in van der Waals clusters. The overall tendency to favor processes in which one vibrational quantum is lost is also typical of predissociation of van der Waals complexes.

In the predissociation of van der Waals complexes, the spectral shift of a vibrational transition is often proportional to the strength of the potential coupling between the intramolecular and van der Waals modes.[39] By analogy, the coupling strength between the NO stretch modes and the dissociative N−N coordinate in $(NO)_2$ may be related to the frequency shift, and hence to the well depths of the $(NO)_2(m = 3, 4)$ complexes. The well depth is defined here as the difference between the energy of the separated $NO(v_a) + NO(v_b)$ product pairs and the energy of the observed vibrational transition in $(NO)_2$. Figure 5 depicts schematically several such plots, where the spin−orbit splitting in $NO(X^2\Pi)$ is suppressed. In the plots, the $NO(v_a) + NO(v_b)$ pairs that correlate with the lowest levels in a local mode description of the NO stretch vibrations, $[v_a, v_b]$, are also shown. Although the observed transitions were assigned using a normal-mode basis where the N−O motions are coupled,

when the NO monomers are at large distance, the coupling between the two NO motions is weakened, and a local-mode model becomes more appropriate. The NO(v_a) + NO(v_b) fragments correlated with the observed $(NO)_2$ vibrational levels were determined from the normal−local mode correlation diagram given elsewhere[40] and are listed in Figure 5. The well depths are given in Table 2 and, as expected, are greater for vibrational levels with multiple quanta of ν_5.

Predissociation. One of the goals of the present work was to find direct or indirect signatures of the participation of the seven electronically excited states, which are calculated at <1 eV in the vertical Franck−Condon region and correlate with ground-state NO($X^2\Pi$) products. The vibrational levels of b_2 symmetry excited in this study may couple to the $^3A_2$ excited electronic state by spin−orbit coupling (vertical excitation energy is 4402 cm^{-1}) or to either the $^1B_1$ or $^1A_1$ excited electronic states by Coriolis coupling (vertical excitation energies of 2433 and 3624 cm^{-1}, respectively).[1,2] The similarity of the energy disposal patterns for predissociation via vibrational levels excited at 1800−7300 cm^{-1} argues against state-specific nonadiabatic transitions in the Franck−Condon region. More likely, the couplings between surfaces correlating with $\Pi_{1/2} + \Pi_{3/2}$ and $\Pi_{1/2} + \Pi_{1/2}$ products, which are separated asymptotically by 123 cm^{-1}, take place in the flat, long-range part of the potential near the asymptotic region, where coupling matrix elements have magnitudes similar to the energy separations of surfaces.

Previous studies have shown that $m = 1$, 2 excitations lead to probabilities of producing the excited NO($\Pi_{1/2}$) + NO($\Pi_{3/2}$) channel that range from 0.58 to 0.95.[13,17] Almost no fragments are produced via the $\Pi_{3/2} + \Pi_{3/2}$ channel. With the exception of $3\nu_1 + \nu_5$, which shows a large preference for the lower spin−orbit states, the spin−orbit ratios obtained in the present study following dissociation in the second and third overtone regions ($m = 3$ and 4) are rather similar to those in the $m = 1$ and 2 regions. Thus, the spin−orbit ratios do not show clear trends with increasing NO dimer vibrational excitation, though the $\Pi_{1/2} + \Pi_{3/2}$ channel appears favored in many of the levels, indicating that nonadiabatic interactions can be quite efficient.

This behavior is typical of spin−orbit couplings that take place in the asymptotic region, where several electronic states coalescence toward product channels that are close in energy. For example, in the barrierless unimolecular reaction of several NO-containing molecules (e.g., NO_2, NCNO, *tert*-butyl NO),[41,42] where the rotational and vibrational degrees of freedom are apportioned statistically, the product spin−orbit states are generated with nonstatistical distributions that vary from molecule to molecule with no particular trend. This has been interpreted as an indication that the requisite nonadiabatic transitions take place near the asymptotic region of the potential, after the rovibrational distributions have been established, with the size of the coupling matrix elements and the extent of the crossing seam determining the final outcome.[42]

The mechanism that determines the vibrational and rotational energy disposal in the overtone excitation of the NO dimer is similar to that in vibrational predissociation of van der Waals clusters, despite the covalent nature of the N−N bond. $\Delta v = -1$ processes dominate, and the time scale for dissociation is determined by the coupling between the NO stretch excitation and the N−N reaction coordinate, either directly or via the ONN bend.

The "cold" rotational distributions following overtone stretch excitation can be compared and contrasted with our recent work on the photodissociation of the NO dimer near the NO($A^2\Sigma^+$) + NO($X^2\Pi$) threshold, which takes place on an electronically excited state that is bound by at least 3600 cm^{-1}.[9,10] The product rotational energies from this more strongly bound potential are apportioned rather statistically, as is typical of barrierless vibrational predissociation mechanisms, except that the low-frequency torsional mode couples less effectively to the other modes.[9,10] In contrast, the rotational distributions in ground-state dissociation of the NO dimer, which is bound by 710 cm^{-1}, cannot be interpreted by invoking either statistical or impulsive models.[17]

The low level of product rotational excitation is characteristic of expansion of low-level wave functions of "disappearing vibrational modes" (e.g., bending and torsion) into rotational degrees of freedom.[43] This is also the explanation given for lower parent excitations ($m = 1$, 2), where between 3 and 12% of the available energy is deposited in rotation.[13,17] Referring to excitation channels that derive from $\Delta v = -1$ processes, such as channels 1 and 5 (see below), and assuming that the energy available to rotation is partitioned equally between NO($v = 0$) and NO($v = v_i$) products, which is reasonable for this mechanism, we find that between 14 and 26% of the available energy is deposited in product rotation (Table 3). This suggests that a similar mechanism is responsible for rotational excitation throughout the entire energy range. The rotational energy is higher for the $\Delta v = -2$ process (channel 7), probably because more energy is available for distribution in rotation and translation.

Extending the studies of vibrational predissociation to higher overtones allows us also to examine the relative importance of $\Delta v = -1$ and -2 processes and the disposition of vibrational energy in the two NO moieties. We find that, except for the case of excitation of $3\nu_5$ discussed below, $\Delta v = -1$ processes are dominant and most of the excitation resides in one NO product. A comparison with the self-relaxation of NO(v), in which transient $(NO)_2$ formation is invoked, is instructive.[44−51]

The slightly endothermic vibration-to-vibration (V−V) energy transfer in 300 K NO collisions has long been attributed to long-range multipole interactions between NO collision partners.[44−46] The unusually rapid vibrational-to-translational (V−T) relaxation rate has been explained by strong attractive forces between the NO radicals.[46] Below 80 K, where endothermicity prohibits V−V transfer, V−T energy transfer plays the dominant role.[44,45,50] Specifically, Smith and co-workers studied the vibrational relaxation rates in NO($X^2\Pi$; $v = 3$) + NO($X^2\Pi$; $v = 0$) collisions down to 7 K and found that the relaxation rate increases strongly with *decreasing* temperature. They proposed that transient formation of the NO dimer takes place with lifetimes with respect to predissociation that are sufficiently long for energy transfer to occur.[50] Smith and co-workers concluded that the high relaxation rates were dominated by V−T energy transfer, rather than V−V energy exchange.[50] This explains the dominance of processes in which vibrational excitation is not apportioned statistically among the two NO moieties, such as we observe in $m = 4$ excitation, and suggests that a significant source of NO($v = 1$) from $(NO)_2$($m = 3$) dissociation would be channel 3.

For $m = 3$ excitation, we first discuss $2\nu_1 + \nu_5$ dissociation. In this case the $v = 2/v = 1$ population ratio is quite high (7.3), and the rotational temperatures of $v = 2$ and $v = 1$ are similar (Table 2). Referring to results obtained in $\nu_1 + 3\nu_5$ excitation, in which $\Delta v = -1$ and $\Delta v = -2$ processes are clearly distinguished, we note that the rotational temperature of fragments generated by the $\Delta v = -1$ process is significantly lower than that generated via $\Delta v = -2$. This suggests that the

rather small fraction of $v = 1$ that is generated in $2\nu_1 + \nu_5$ dissociation derives from channel 2 ($\Delta v = -1$) rather than channel 3.

The situation following excitation of $3\nu_5$ is different. Here, the vibrational population is divided equally between $v = 2$ and $v = 1$, and the rotational temperature of $v = 1$ is higher than that of $v = 2$, as is more typical of $\Delta v = -2$ processes. We therefore suggest that the contribution of channel 3 to $3\nu_5$ dissociation is larger than that in $2\nu_1 + \nu_5$. It is plausible that dissociation involving multiple quanta of ν_5, a mode that is coupled more strongly to the bending mode and the N−N reaction coordinate than ν_1, results in stronger coupling that also facilitates the $\Delta v = -2$ pathway, as observed also in $\nu_1 + 3\nu_5$ dissociation.

V. Summary

The IR predissociation of the NO dimer was studied in the region 4000−7400 cm^{-1} via REMPI detection of NO($X^2\Pi_{1/2,3/2}$; $v = 1, 2, 3$) products. Photofragment spectra obtained by monitoring NO($X^2\Pi_{3/2}$; $v = 1, 2, 3$) products reveal four vibrational bands, which are assigned as $3\nu_5$, $2\nu_1 + \nu_5$, $\nu_1 + 3\nu_5$, and $3\nu_1 + \nu_5$. The observed levels involve only excitation of NO stretch modes. The predissociation rates appear not to depend strongly on the excited vibrational level and are of the same order of magnitude as the corresponding rates for $2\nu_5$ and $\nu_1 + \nu_5$. The rate-determining step is probably V−T coupling, as it is in the reverse process—the self-relaxation of NO(v) at low temperatures.

Vibrational, rotational, and spin−orbit distributions were determined for all of the observed product NO states. The major dissociation pathway involves $\Delta v = -1$, as is typical of systems where the coupling between the high- and low-frequency modes is weak. $\Delta v = -2$ processes are more prevalent in predissocation of levels with a large number of quanta of the asymmetric NO stretch mode ν_5 (i.e., $3\nu_5$ and $\nu_1 + 3\nu_5$), which are more strongly coupled to the N−N dissociation coordinate.

In dissociation from $\nu_1 + 3\nu_5$ and $3\nu_1 + \nu_5$, vibrational excitation is confined to one NO product. In contrast, in dissociation from $3\nu_5$ and $2\nu_1 + \nu_5$, vibrational energy can be distributed in channels with one or two NO($v = 1$) products. On the basis of trends in energy disposal, we suggest that in predissociation of $3\nu_5$, NO($v = 1$) originates in both $\Delta v = -1$ and $\Delta v = -2$ processes, while the former is the main source of NO($v = 1$) in $2\nu_1 + \nu_5$ dissociation.

The products' spin−orbit ratios show a slight preference for the ground $X^2\Pi_{1/2}$ level, and in analogy with previous results, it is suggested that the dominant channel is $X^2\Pi_{1/2} + X^2\Pi_{3/2}$. The similarity of the spin−orbit ratios in excitation of most of the NO dimer vibrational states points to the long-range part of the potential in the N−N coordinate as the locus of nonadiabatic transitions to electronic states correlating with excited product spin−orbit states. Thus, it appears that vibrational nonadiabatic coupling following V−T transfer takes place at shorter N−N separations, while the spin−orbit ratios are determined at long range, where several potential curves coalesce. No evidence of direct excitation to electronic states whose vertical energies lie in this energy region is obtained.

Acknowledgment. We thank Lin Feng and Vladimir Dribinski for many helpful discussions. Support by the National Science Foundation and the donors of the Petroleum Research Fund, administered by the American Chemical Society, is gratefully acknowledged.

References and Notes

(1) Tobita, M.; Perera, S. A.; Musial, M.; Bartlett, R. J.; Nooijen, M.; Lee, J. S. *J. Chem. Phys.* **2003**, *119*, 10713.
(2) East, A. L. L. *J. Chem. Phys.* **1998**, *109*, 2185.
(3) Ha, T. K. *Theor. Chim. Acta* **1981**, *58*, 125.
(4) Sayos, R.; Valero, R.; Anglada, J. M.; Gonzalez, M. *J. Chem. Phys.* **2000**, *112*, 6608.
(5) Forte, E.; Van Den Bergh, H. *Chem. Phys.* **1978**, *30*, 325.
(6) Billingsley, J.; Callear, A. B. *Trans. Faraday Soc.* **1971**, *67*, 589.
(7) Kukolich, S. G. *J. Mol. Spectrosc.* **1983**, *98*, 80.
(8) Western, C. M.; Langridge-Smith, P. R. R.; Howard, B. J.; Novick, S. E. *Mol. Phys.* **1981**, *44*, 145.
(9) Dribinski, V.; Potter, A. B.; Fedorov, I.; Reisler, H. *Chem. Phys. Lett.* **2004**, *385*, 233.
(10) Potter, A. B.; Dribinski, V.; Demyanenko, A. V.; Reisler, H. *J. Chem. Phys.* **2003**, *119*, 7197.
(11) Casassa, M. P.; Woodward, A. M.; Stephenson, J. C.; King, D. S. *J. Chem. Phys.* **1986**, *85*, 6235.
(12) Casassa, M. P.; Stephenson, J. C.; King, D. S. *J. Chem. Phys.* **1986**, *85*, 2333.
(13) Casassa, M. P.; Stephenson, J. C.; King, D. S. *J. Chem. Phys.* **1988**, *89*, 1966.
(14) Tachibana, A.; Suzuki, T.; Yamato, M.; Yamabe, T. *Chem. Phys.* **1990**, *146*, 245.
(15) Tachibana, A.; Yamato, M.; Suzuki, T.; Yamabe, T. *J. Mol. Struct.−Theochem* **1991**, *231*, 291.
(16) Matsumoto, Y.; Ohshima, Y.; Takami, M. *J. Chem. Phys.* **1990**, *92*, 937.
(17) Hetzler, J. R.; Casassa, M. P.; King, D. S. *J. Phys. Chem.* **1991**, *95*, 8086.
(18) Mason, J. *J. Chem. Educ.* **1975**, *52*, 445.
(19) East, A. L. L.; McKellar, A. R. W.; Watson, J. K. G. *J. Chem. Phys.* **1998**, *109*, 4378.
(20) Asselin, P.; Soulard, P.; Lacome, N. *J. Mol. Spectrosc.* **1998**, *190*, 274.
(21) Brechignac, P.; Debenedictis, S.; Halberstadt, N.; Whitaker, B. J.; Avrillier, S. *J. Chem. Phys.* **1985**, *83*, 2064.
(22) Dinerman, C. E.; Ewing, G. E. *J. Chem. Phys.* **1970**, *53*, 626.
(23) Dkhissi, A.; Soulard, P.; Perrin, A.; Lacome, N. *J. Mol. Spectrosc.* **1997**, *183*, 12.
(24) Dkhissi, A.; Lacome, N.; Perrin, A. *J. Mol. Spectrosc.* **1999**, *194*, 156.
(25) McKellar, A. R. W.; Watson, J. K. G.; Howard, B. J. *Mol. Phys.* **1995**, *86*, 273.
(26) McKellar, A. R. W.; Watson, J. K. G. *J. Mol. Spectrosc.* **1999**, *194*, 229.
(27) Menoux, V.; Ledoucen, R.; Haeusler, C. *Can. J. Phys.* **1984**, *62*, 322.
(28) Watson, J. K. G.; McKellar, A. R. W. *Can. J. Phys.* **1997**, *75*, 181.
(29) Brookes, M. D.; McKellar, A. R. W.; Amano, T. *J. Mol. Spectrosc.* **1997**, *185*, 153.
(30) Krim, L. *J. Mol. Struct.* **1998**, *471*, 267.
(31) Krim, L.; Lacome, N. *J. Phys. Chem. A* **1998**, *102*, 2289.
(32) Nour, E. M.; Chen, L. H.; Strube, M. M.; Laane, J. *J. Phys. Chem.* **1984**, *88*, 756.
(33) Conroy, D.; Aristov, V.; Feng, L.; Reisler, H. *J. Phys. Chem. A* **2000**, *104*, 10288.
(34) Barnes, W. L.; Susskind, J.; Hunt, R. H.; Plyler, E. K. *J. Chem. Phys.* **1972**, *56*, 5160.
(35) Tikhonov, A. N. *Sov. Math. Dokl.* **1963**, *4*, 1035.
(36) Mohlmann, G. R.; van Sprang, H. A.; Bloemen, E.; de Heer, F. J. *Chem. Phys.* **1978**, *32*, 239.
(37) Judge, R. H.; Clouthier, D. J. *Comput. Phys. Commun.* **2001**, *135*, 293.
(38) Demyanenko, A. V.; Potter, A. B.; Dribinski, V.; Reisler, H. *J. Chem. Phys.* **2002**, *117*, 2568.
(39) Le Roy, R. J.; Davies, M. R.; Lam, M. E. *J. Phys. Chem.* **1991**, *95*, 2167.
(40) Mills, I. M.; Robiette, A. G. *Mol. Phys.* **1985**, *56*, 743.
(41) Reisler, H.; Noble, M.; Wittig, C. Photodissociation Processes in NO-Containing Molecules. In *Molecular Photodissociation Dynamics*; Ashfold, M. N. R., Baggott, J. E., Eds.; Royal Society of Chemistry: London, 1987.
(42) Reid, S. A.; Reisler, H. *J. Phys. Chem.* **1996**, *100*, 474.
(43) Schinke, R. *Photodissociation Dynamics*; Cambridge University Press: Cambridge, 1993.
(44) Islam, M.; Smith, I. W. M.; Wiebrecht, J. W. *J. Phys. Chem.* **1994**, *98*, 9285.
(45) Wysong, I. J. *J. Chem. Phys.* **1994**, *101*, 2800.
(46) Horiguchi, H.; Tsuchiya, S. *Jpn. J. Appl. Phys.* **1979**, *18*, 1207.
(47) Stephensen, J. C. *J. Chem. Phys.* **1974**, *60*, 4289.
(48) Stephenson, J. C. *J. Chem. Phys.* **1973**, *59*, 1523.
(49) Nikitin, E. E. *Opt. Spectrosc.* **1960**, *9*, 8.
(50) James, P. L.; Sims, I. R.; Smith, I. W. M. *Chem. Phys. Lett.* **1997**, *276*, 423.
(51) Wysong, I. J. *Chem. Phys. Lett.* **1994**, *227*, 69.